Microtubule Protofilament Number Is Modulated in a Stepwise Fashion by the Charge Density of an Enveloping Layer

Uri Raviv,*† Toan Nguyen,‡ Rouzbeh Ghafouri,‡ Daniel J. Needleman,*† Youli Li,*† Herbert P. Miller,† Leslie Wilson,† Robijn F. Bruinsma,‡ and Cyrus R. Safinya*†

*Materials Department, Physics Department, and †Molecular, Cellular, and Developmental Biology Department, Biomolecular Science and Engineering Program, University of California, Santa Barbara, California; and ‡Department of Physics and Astronomy, University of California, Los Angeles, California

ABSTRACT Microtubules are able to adjust their protofilament (PF) number and, as a consequence, their dynamics and function, to the assembly conditions and presence of cofactors. However, the principle behind such variations is poorly understood. Using synchrotron x-ray scattering and transmission electron microscopy, we studied how charged membranes, which under certain conditions can envelop preassembled MTs, regulate the PF number of those MTs. We show that the mean PF number, $\langle N \rangle$, is modulated primarily by the charge density of the membranes. $\langle N \rangle$ decreases in a stepwise fashion with increasing membrane charge density. $\langle N \rangle$ does not depend on the membrane-protein stoichiometry or the solution ionic strength. We studied the effect of taxol and found that $\langle N \rangle$ increases logarithmically with taxol/tubulin stoichiometry. We present a theoretical model, which by balancing the electrostatic and elastic interactions in the system accounts for the trends in our findings and reveals an effective MT bending stiffness of order 10–100 $k_B T$/nm, associated with the observed changes in PF number.

INTRODUCTION

Microtubules (MTs) are anionic polymers that self-assemble from tubulin protein subunits into hollow cylinders. Tubulin dimers are arranged head to tail in protofilaments (PFs) that interact laterally and form the MT wall. In eukaryotic cells, a 13-PF arrangement is by far the most common (1), though MTs with 11, 12, 14, and 15 PFs have been observed (2). For example, it has been found (3) that the formation of MT with more than 13 PFs in the ciliate *Nyctotherus ovalis* Leidy is a highly ordered process. Such MTs are restricted to the nucleoplasm and, moreover, to later stages of nuclear division. They assemble during the anaphase of micronuclear mitosis and during the elongation phase of macronuclear division. About 85% of the MTs that form the large MT bundles assemble in *Drosophila* wing epidermal cells after the cells have lost their centrosomal MT-organizing centers composed of 15 PFs (4,5).

When MTs interact with MT-associated proteins or other cofactors they are able to adjust their structure dynamically and self-assemble into bundles and several alternative structures, which are critical components in a broad range of cell functions (6–18). Although it is well known that MTs are able to adjust their PF number, N, and, as a consequence, their dynamics and function, to assembly conditions such as pH, the presence of cofactors, drugs, and MT-associated proteins (3,8–10,19–24) or the number of successive disassembly-assembly cycles (2), the principle behind those variations is poorly understood. It is also unclear how the PF number is kept at 13 in cells at high fidelity (1,2).

In earlier articles (16,25), we studied the interactions between cationic liposomes and MTs. We established the conditions under which the cationic membranes can coat the MTs and form lipid-protein nanotubes (LPN). The LPNs exhibit a rather remarkable architecture, with the cylindrical lipid bilayer sandwiched between a MT and outer tubulin oligomers, forming rings or spirals (Fig. 1). The unique type of self-assembly arises because of a mismatch between the charge densities of the negatively charged MT and the cationic lipid bilayer.

Here, we study in detail, using small angle synchrotron x-ray diffraction (SAXRD) and transmission electron microscopy (TEM), how the mean PF number, $\langle N \rangle$, of a preassembled MT is influenced by the tunable properties of an enveloping cationic membrane, which forms the LPNs. We show that the mean PF number, $\langle N \rangle$, is modulated primarily by the charge density of the membrane, σ. $\langle N \rangle$ decreases in a stepwise fashion with increasing σ, toward the value of the uncoated MT, at high σ. $\langle N \rangle$ does not depend on the membrane-protein stoichiometry or the solution ionic strength. We suggest that the LPN structure demonstrates that $\langle N \rangle$ and perhaps, as a consequence, MT dynamics, are determined by the attempt of the system to optimize the match between the charge density of the MT wall and that of the layer coating it, which in vivo would primarily consist of MT-associated proteins. Finally, we describe a quantitative physical model to account for our observations, from which we estimate that the

Submitted May 9, 2006, and accepted for publication September 5, 2006.

Address reprint requests to Uri Raviv at his present address, Physical Chemistry Department, The Institute of Chemistry, The Hebrew University of Jerusalem, Givat Ram, 91904, Israel. Tel.: 972-2-6585325; Fax: 972-2-5660425; E-mail: raviv@chem.ch.huji.ac.il; or to Cyrus R. Safinya, Materials Research Laboratory, UCSB, Santa Barbara, CA 93106. Tel.: 805-893-8635; Fax: 805-893-7221; E-mail: safinya@mrl.ucsb.edu.

Daniel J. Needleman's present address is Harvard Medical School, Harvard University, Boston, MA 02115.

0006-3495/07/01/278/10 $2.00

doi: 10.1529/biophysj.106.087478

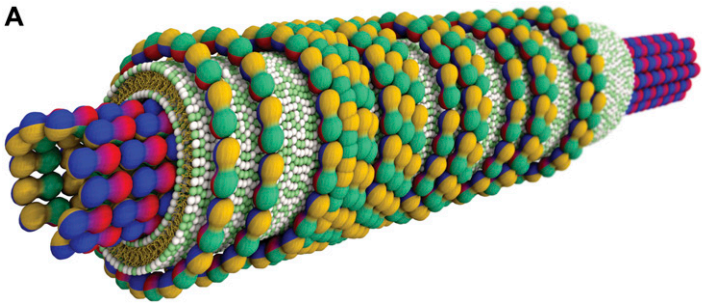

FIGURE 1 (*A*) A side-view cartoon of the LPN structure showing a microtubule made of tubulin protein subunits (*red-blue-yellow-green objects*) coated by a lipid bilayer (with yellow tails and green/white headgroups), which in turn is coated by a third layer of tubulin oligomers exposing the side that in MT is facing the lumen. (*B*) A top-view cartoon of the LPN structure.

effective bending stiffness associated with variation in PF number is of order 10 k_BT/nm.

MATERIALS AND METHODS

Tubulin was purified from bovine brains as described elsewhere(14,26). Tubulin concentrated to 45 ± 5 μM in PEM buffer (50 mM 1,4-piperazinediethanesulfonic acid, 1 mM $MgCl_2$, 1 mM EGTA, 0.02% (w/v) NaN_3, adjusted to pH 6.8 with ~70 mM NaOH), 1 mM guanosine triphosphate (GTP), and 5% glycerol was incubated at 36 ± 1°C for 20 min, as described (14,16–18,26,27). Unless otherwise indicated, MT depolymerization was suppressed by adding the chemotherapy drug taxol at 1:1 tubulin/taxol molar ratio (20,28). Liposome solutions were prepared by mixing the cationic lipid, dioleoyl($C_{18:1}$) trimethyl ammonium propane (DOTAP) with the homologous neutral lipid, dioleoyl($C_{18:1}$) phosphatidylcholine (DOPC) (Avanti Polar Lipids), at a total lipid concentration of 30 mg/ml in Millipore water (18.2 MΩ cm), as described (29). The mole fraction of cationic lipids is given by

$$x_{CL} \equiv N_{CL}/(N_{CL} + N_{NL}), \quad (1)$$

where N_{CL} and N_{NL} are the numbers of cationic and neutral lipids, respectively. The relative cationic lipid/tubulin stoichiometry, $R_{CL/T}$, is defined as

$$R_{CL/T} \equiv N_{CL}/N_T, \quad (2)$$

where N_T is the number of tubulin dimers. Lipid solutions were diluted so that equal volumes of preassembled MTs and liposome solutions could be mixed to yield the desired lipid/tubulin stoichiometry. The resulting complexes were characterized by SAXRD and TEM, as described (14–18). The following results are based on several different experiments, using different tubulin purification preparations and liposome solutions.

Samples were not oriented; thus, SAXRD scans collected on a 2D detector were azimuthally averaged to yield scattering intensity as a function of momentum transfer, q (Fig. 2, *C* and *D*). To model the data, as in other MT-related scattering studies (14,16–20,22,30), a series of power laws that pass through the minima of the scattering intensities was subtracted (Fig. 2 *D*). The assumption here is that the size distribution is very narrow within each sample.

RESULTS AND DISCUSSION

TEM images (Fig. 2 *A*) and SAXRD measurements (Fig. 2, *C–E*) performed on pure MT solutions are in agreement with earlier studies (14–18,20,22,31). The SAXRD profile of MTs is consistent with the form factor of an isotropic hollow

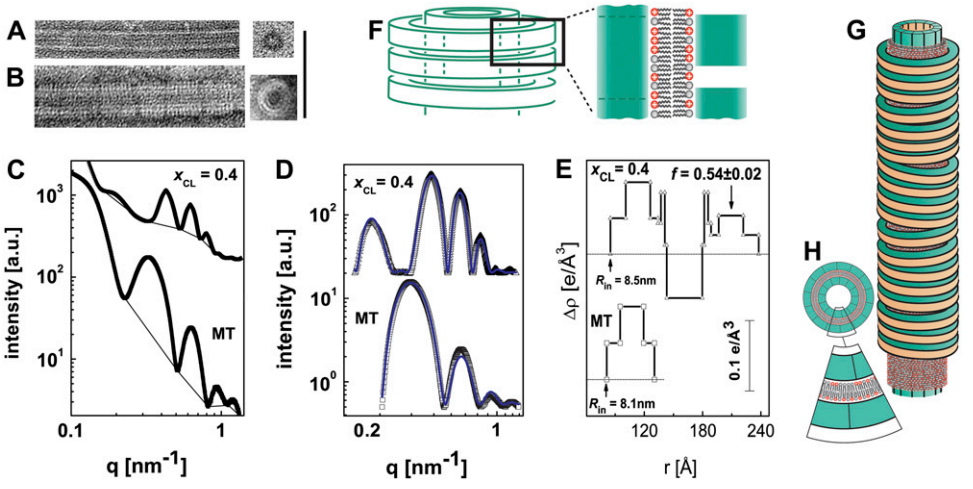

FIGURE 2 TEM images, SAXRD scans, and analysis of MTs and MTs complexed with DOTAP/DOPC membranes (see Materials and Methods). (*A*) TEM images of an MT. A whole-mount image is on the left side and a cross section is shown on the right. (*B*) TEM image of an LPN. The mole fraction of charged lipids, $x_{CL} \equiv N_{CL}/(N_{CL} + N_{NL}) = 0.5$, and the cationic lipid/tubulin stoichiometry, $R_{CL/T} \equiv N_{CL}/N_T = 120$. N_{CL} and N_{NL} are the numbers of cationic and neutral lipids, respectively, and N_T is the number of tubulin dimers. A whole mount image is on the left side and a cross section, showing an inner MT with 14 PFs, is on the right. We note that we did not perform a statistical study of such TEM cross section, as our x-ray data is a bulk measurement and inherently includes statistics. The vertical scale bar corresponds to 100 nm. (*C*) Azimuthally averaged raw SAXRD data (*solid symbols*) of MTs and LPNs with $x_{CL} = 0.4$ and $R_{CL/T} = 40$, as indicated in the figure. Each broken line is a series of power laws that pass through the minima of the scattering intensities. As in other MT-related scattering studies(14,16,20,22), this is the assumed background scattering. (*D*) SAXRD data from *C*, following background subtraction (*open symbols*). The blue solid curves are the fitted scattering models. (*E*) The variation of the radial electron density, $\Delta\rho(r)$, relative to water (*dotted lines*), of MT and LPN walls, as obtained from fitting the data in *C* to models of isotropic infinitely-long hollow cylinders with nonuniform electron density profile. r is the distance from the center of the cylinders. The fraction of tubulin oligomer coverage at the external LPN wall relative to the internal MT wall, f, obtained from fitting the model to the data, is indicated in the figure. The inner radius, R_{in}, of the MT wall and that of the internal MT within the LPN complex, obtained from the fitting, are also indicated. (*F*) A schematic that represents a vertical cut through the LPN wall, corresponding to the top radial electron density profile in *E*. (*G*) A cartoon of the LPN. (*H*) A cartoon of a cross section of the LPN and a magnified slice.

cylinder (Fig. 2 *D*). Based on MT structural data (31,32), we modeled the MT as three concentric cylindrical shells of a high-electron-density region surrounded by two of low electron density, as shown in Fig. 2 *E*, keeping the total wall thickness, $a_1 = 4.9$ nm, and mean electron density the same as those of MTs. The thickness and location of the high-electron-density region, within the MT wall, and the inner MT radius, R_{in}, are fitting parameters in this model (see Appendix for details).

TEM images (Fig. 2 *B*) reveal that when MTs were mixed with cationic liposomes, unique three-layered LPNs formed. The LPN consists of a MT that is coated by a lipid bilayer (it appears brighter in the images, as the ionic stain avoids the hydrophobic lipid tails), which in turn is coated by tubulin oligomers, made of curved PFs in helical arrangement with different pitches or stacks of rings (Fig. 1). The LPN appears to be the best the system can do to optimize its electrostatic interactions. The formation of tubulin oligomers at the external layer is enabled because the cationic membranes lead to MT depolymerization, resulting in curved PFs. By using a slowly-hydrolyzable GTP analog, GMPCPP, the formation of tubulin oligomers at the external layer of the LPN is prevented (U. Raviv, D. J. Needleman, Y. Li, H. P. Miller, L. Wilson, and C. R. Safinya, unpublished data). It is of interest to note that the kinetochore is believed to recognize and maintain its attachment to the plus-end of spindle MT by a similar three-layered tubular structure induced by MT-associated protein complexes (6,7). The protein rings that coat the MT allow the attachment of the kinetochore to the spindle MT, whereas the internal MT is able to maintain independently the dynamics required for cell division.

A typical SAXRD scan of the MT-lipid complexes is shown in Fig. 2 *C*. The broad oscillations are different from that of MTs and correspond to the form factor of the LPNs. To gain quantitative insight into the structure of the complexes, we analyzed the background-subtracted SAXRD data, shown in Fig. 2 *D*, by fitting to a model. We extended the isotropic concentric cylindrical shells model of MTs to include the second lipid bilayer and the third tubulin layer (Fig. 2, *E* and *F*). The radial electron density profile of the inner MT wall and outer tubulin monolayer are taken from the fit to the MT scattering data. The third tubulin layer is assumed to have the mirror image of the inner MT-wall radial electron-density profile, i.e., the PF side directed inward in the MT should be directed outward in the external tubulin layer (8) (Fig. 1). See Appendix for details. Apart from providing a good fit to the scattering data, the main supporting evidence for this assumption is the fact that we never found, even in the presence of excess lipids, subsequent external lipid bilayers or lipids inside the MT lumen, showing that both surfaces are similar and have low propensity to interact with cationic liposomes. The electron-density profiles of the lipid bilayer are taken from literature data (33,34). Using three different lipid solutions with different tail lengths (data not shown), we obtained the expected shifts in the form factor, indicating that we have identified correctly the location of the lipid bilayer. Finally, there are two free parameters in our model: The inner MT radius, R_{in}, which is allowed to fluctuate within physical reasonable limits and the fraction of tubulin coverage, f, at the external layer, relative to the inner MT wall, which is allowed to float freely between 0 and 1. The scattering model (Fig. 2 *D*) fits very well to the data.

We are able to control the charge density of the layer that coats the MT and this, based on our observations described below, is a key physical parameter. The membrane charge density, σ, is set by the bilayer thickness, $a_2 \sim 4$ nm, the area per lipid headgroup (29), $A_0 \sim 0.7$ nm^2, for both lipids, and can be tuned by the mole fraction of cationic lipids, $x_{CL} \equiv N_{CL}/(N_{CL} + N_{NL})$, where N_{CL} and N_{NL} are the numbers of cationic and neutral lipids, respectively. When all the lipids are cationic $\sigma = \sigma_{cat} = 2e/a_2A_0$, where e is the charge of an electron. In general, $\sigma \equiv x_{CL}\sigma_{cat.}$ The relative charged-membrane/tubulin stoichiometry, $R_{CL/T}$, is given by, $R_{CL/T} \equiv N_{CL}/N_T$, where N_T is the number of tubulin dimers. $R_{CL/T}$ can be tuned to control the overall charge of the complex. $R_{CL/T} \approx 40$ corresponds to the mixing isoelectric point.

Fig. 3 summarizes a series of SAXRD scans as in Fig. 2*C*, analyzed as in Fig. 2, *D* and *E*. In Fig. 3 *A*, f is plotted as a function of x_{CL} (or σ) at various $R_{CL/T}$ values. The coverage of the third layer arises primarily from the mismatch between the charge density of the membrane and the MT wall but also due to the mixing entropy of the lipids within the bilayer. There is no difference in the electrostatic energy if the cationic lipid neutralizes the MT or the external tubulin oligomers. When σ is smaller than the charge density of the MT wall, $\sigma_{MT} = 0.2\ e/\text{nm}^3$, mixing entropy, which favors random distribution of the charged lipids across the bilayer (35), induces coating of tubulin oligomers, yielding $f > 0.4$ even at low σ. As σ increases, more charged lipids can go to the external monolayer, enable the adsorption of more tubulin oligomers, and account for the monotonic increase in f. Unlike σ, the stoichiometry, $R_{CL/T}$, has little effect on f.

The internal MT size is determined by R_{in}. $\langle N \rangle$ was calculated from R_{in} (Fig. 3 *B*), assuming (8.10) that the width of a tubulin subunit (31), $2a = 5$ nm, remains constant at the MT wall center, $R_{in} + a_1/2$: $\langle N \rangle \equiv 2\pi(R_{in} + a_1/2)/2a$. If we assume that the width of a tubulin subunit remains constant at R_{in} ($2\pi R_{in}/13 \approx 4$ nm) or at $R_{in} + a_1$ ($2\pi(R_{in} + a_1)/13 \approx 6$ nm), the values of $\langle N \rangle$ could change by no more than 1.5%. R_{in} is obtained directly from fitting the model to the data as described. However, R_{in} could also vary, by up to 1%, if other assumptions are made to the model, for example, if a_1 is allowed to be a function of R_{in} while keeping the volume of a tubulin subunit constant, and the surface area of tubulin remains constant at R_{in} or $R_{in} + a_1$. Those variations are smaller than the scatter in the data. Finally, R_{in} is obtained from bulk measurements that benefit from good statistics and are highly reproducible and reliable (Fig. 3 *B*).

R_{in} (or $\langle N \rangle$) are plotted, in Fig. 3 *B*, as a function of x_{CL} (or σ) at various $R_{CL/T}$ values. We find that $\langle N \rangle$ decreases

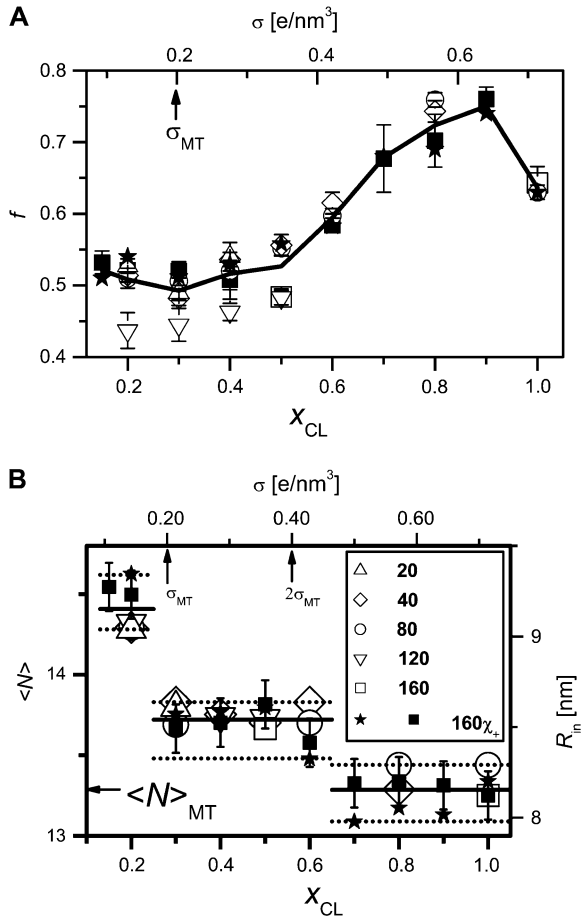

FIGURE 3 States diagrams of the LPNs as a function of the mole fraction of cationic lipids, x_{CL}, or the membrane charge density, σ (*top horizontal axis*); σ is calculated from x_{CL} as explained in Results and Discussion. The MT wall charge density, σ_{MT}, as estimated based on the primary structure of tubulin (15,16,31,40), is indicated. Each data point is obtained from scattering data and fitting to a model, as demonstrated in Fig. 2. Different symbols correspond to different charged lipid/tubulin ratios, $R_{CL/T}$, as indicated in Fig. 3 *B* (*inset*). For all data points shown, there are enough lipids to cover each MT with a bilayer. Solid symbols, for which $R_{CL/T} = 160 \cdot x_{CL}$, correspond to a series of data points at which the total number of lipids/tubulin is kept constant and is exactly enough to coat each MT with a bilayer (calculated as in May and Ben-Shaul (35)). (*A*) Fraction of tubulin oligomer coverage at the external layer, f, as a function of x_{CL} (or σ). The solid line indicates the mean values of $f(x_{CL})$. (*B*) The inner wall radius, R_{in}, of the internal MT within the LPN complex and mean PF number, $\langle N\rangle$, as a function of x_{CL} (or σ). R_{in} is obtained from fitting the scattering data to the model, whereas $\langle N\rangle$ is estimated from R_{in} (see Results and Discussion). The arrow indicates the $\langle N\rangle$ value of pure MTs, $\langle N\rangle_{MT} = 13.3$, as obtained from the fit to the MT form factor, shown in Fig. 2, in good agreement with earlier work (14,15,20,22). The three solid lines indicate the mean values of $\langle N\rangle$ at each step. The broken lines indicate the maximum and the minimum values of $\langle N\rangle$ at each step.

discontinuously with σ and exhibits two steps, within the experimental accessible σ range. At $\sigma < \sigma_{MT}$, $R_{in} = 9.02 \pm 0.11$ nm and $\langle N\rangle = 14.40 \pm 0.15$. At $\sigma_{MT} < \sigma \leq 2.15\sigma_{MT}$, $R_{in} = 8.48 \pm 0.08$ nm and $\langle N\rangle = 13.72 \pm 0.09$, and finally at $\sigma > 2.15\sigma_{MT}$, $R_{in} = 8.13 \pm 0.09$ nm and $\langle N\rangle = 13.28 \pm 0.12$, which is similar to values we (14,15,17,18) and others (2,20,22) obtained for taxol-stabilized MTs. The nonintegral nature of $\langle N\rangle$ results from the fact the x-ray data provides the mean PF number. So the variation in the mean PF number is in fact a variation in the distribution of PF numbers. $\langle N\rangle$ values of 14.4, 13.72, and 13.28 correspond to the high percentage of MTs with 15, 14, and 13 PFs, respectively. As we found for f, the lipid/protein stoichiometry ratio, $R_{CL/T}$, has little effect on R_{in} (or $\langle N\rangle$), and it is again σ that turns out to be the key parameter. Decreasing $\langle N\rangle$ with σ appears to be the best the system can do to neutralize itself and compensate for the charge-density mismatch between the MT and the lipid bilayer. As R_{in} or $\langle N\rangle$ decrease, the angle between the PFs decreases and they expose a larger fraction of their surface to the lipid layer and thereby are able to neutralize more cationic lipids.

By mixing DOTAP with the neutral lipid dioleoyl($C_{18:1}$) phosphatidylethanolamine (DOPE), which has a smaller headgroup than that of DOPC, we obtained negative membrane spontaneous curvatures (36). The cationic lipid dilauryl ($C_{12:0}$) trimethyl ammonium propane (DLTAP) and the homologous neutral lipid dilauryl($C_{12:0}$) phosphatidylcholine (DLPC) (Avanti Polar Lipids) have shorter hydrophobic tailgroups (~1.2 nm) compared to DOTAP/DOPC (~1.4 nm). As the bending rigidity of a fluid membrane (37,38), κ, is given by $\kappa \propto (a_2)^3$, where a_2 is the membrane thickness, DLTAP/DLPC membranes have ~60% lower κ compared to DOTAP/DOPC membranes. Fig. 4, *A* and *C*, shows that when MTs are complexed with DLTAP/DLPC or DOTAP/DOPE membranes, the behavior is to a great extent similar to that obtained with DOTAP/DOPC membranes, the main difference being when $\sigma \approx \sigma_{MT}$, where the boundaries between the steps may have shifted a bit. This indicates that although the energy barrier for the formation of the LPN is a function of κ (16), once the LPN has formed, the charge density is the key parameter in determining $\langle N\rangle$.

Similarly, for $x_{CL} = 0.5$, the addition of salt has, within the scatter, no effect on R_{in} (or $\langle N\rangle$) (Fig. 4 *A*). This is attributed to the fact that at the interface between the internal MT and the lipid bilayer, the complex is highly charged and the ion concentration is a few molar and therefore not sensitive to small variation in the solution ionic strength outside the complex, which is at a much lower concentration. However, the addition of salt significantly increases f (Fig. 4, *B* and *C*), because it screens the electrostatic repulsion between the negatively charged tubulin oligomers, which are exposed to the salt solution. This is the way to achieve full tubulin coverage at the external layer (without added salt, $f < 0.8$, see Fig. 3 *A*). Above some critical salt concentration, which increases with x_{CL}, the complexes do not form (indicated by $f = 0$ in Fig. 4, *B* and *C*), because at high salt concentration the propensity of the solution to accept more counterions is reduced and thus counterion release, which is the driving force for the complex formation (36), is not favorable.

The fact that, within the scatter, R_{in} (or $\langle N\rangle$) is stationary, whereas f changes dramatically, in the presence of salt (Fig.

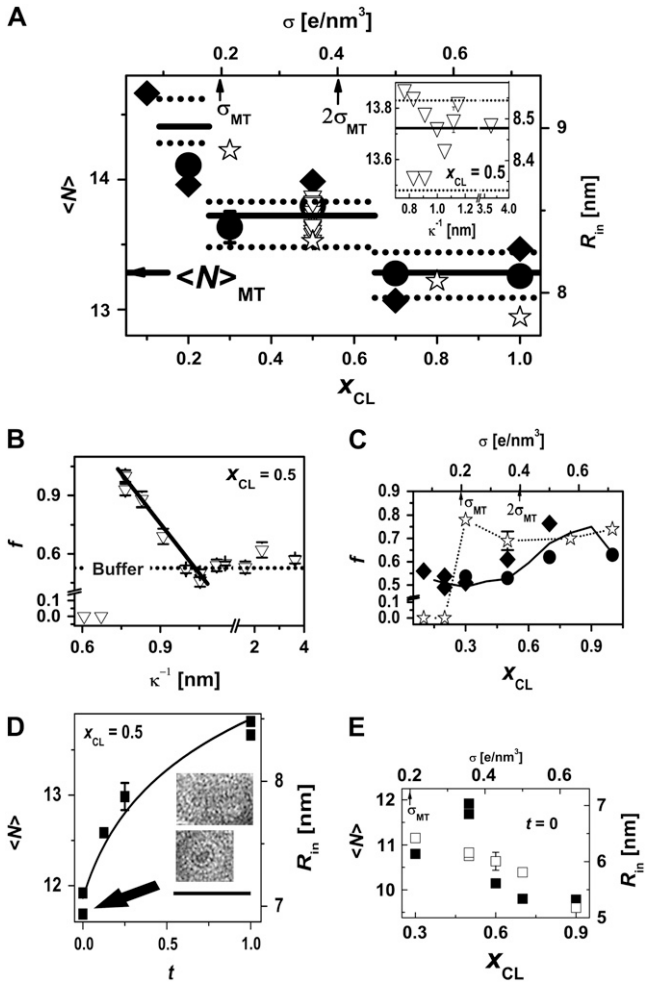

FIGURE 4 The effect of salt, taxol, and membrane spontaneous curvature and rigidity on the mean PF number, $\langle N \rangle$, and tubulin oligomer coverage, f. The cationic lipid/tubulin stoichiometry $R_{CL/T} = 160 \cdot x_{CL}$ for all data points. (*A*) $\langle N \rangle$ (or R_{in}) as a function of x_{CL} (or σ). The solid and broken lines are taken from Fig. 3 *B*, indicating the mean values of $\langle N \rangle$ and the upper and lower limits of $\langle N \rangle$ at each step, respectively, for MTs complexed with DOTAP/DOPC membranes. Solid diamonds indicate the $\langle N \rangle$ values of MTs complexed with DLTAP/DLPC membranes and solid circles indicate the values for MTs complexed with DOTAP/DOPE membranes. Open symbols indicate the effect of added salt when MTs are complexed with DOTAP/DOPC membranes. Stars indicate the addition of 50 mM KCl (leading to Debye length of $\kappa^{-1} = 0.9$ nm, when the buffer is taken into account) at several membrane charge densities. Triangles indicate the addition of different salt concentrations when $x_{CL} = 0.5$. The inset shows the variation of $\langle N \rangle$ with κ^{-1}, when $x_{CL} = 0.5$. (*B*) The variation of f with κ^{-1} (i.e., salt) for $x_{CL} = 0.5$, for MTs complexed with DOTAP/DOPC membranes. The broken line indicates the mean value of f for the complexes in the buffer solution with no added salt. The solid line is a guide for the eye. (*C*) f as a function of x_{CL}. The solid line is taken from Fig. 3 *A*. Other symbols are as in Fig. 4 *A*. (*D*) $\langle N \rangle$ (or R_{in}) as a function of the molar ratio, t, between taxol and tubulin for $x_{CL} = 0.5$ with DOTAP/DOPC membranes. The solid line is a fit to a logarithmic expression: $\langle N \rangle = \ln(142218 + 883725 \times t)$. The inset is a TEM cross section (*bottom*) corresponding to $t = 0$ (*arrow*), showing the inner MT with 12 PFs and a TEM side-view image (*top*) showing a short LPN. (Scale bar, 50 nm.) We note that we did not perform a statistical study of such TEM cross sections, as our x-ray data is a bulk measurement and inherently includes statistics. (*E*) $\langle N \rangle$ (or R_{in}) as a function of x_{CL} (or σ) for $t = 0$, corresponding to no added taxol. Open squares correspond to tubulin, which was directly mixed with DOTAP/DOPC membranes (with no added GTP). Solid squares correspond to DOTAP/DOPC membranes that were mixed with MTs polymerized with GTP at 36 ± 1°C but not taxol-stabilized.

4, *A* and *B*) shows unambiguously that the coverage of tubulin oligomers has little effect on $\langle N \rangle$ and it is σ that predominantly controls the MT PF number. This may well be due to the diameter of the tubulin rings or spirals at the external layer, which happens to be similar to the diameter of free tubulin rings in solution (30), implying that the rings do not exert large tension on the internal MT. The membrane bending rigidity, κ, sets an energy barrier for the formation of the LPN (16). However, once the LPN is formed, it seems that the bending rigidity and spontaneous curvature of the membrane do not play a role, within our experimental conditions. We may conclude that the elastic properties of the layer that coats the MT in the LPN have, to a certain degree, little effect on $\langle N \rangle$ compared to the membrane charge density.

We thus used the LPN system to examine the effect of the chemotherapy drug taxol, which is known to stabilize MTs (15,19,20,28). Without taxol, similar LPNs are obtained and R_{in} (or $\langle N \rangle$) again decreases with σ (Fig. 4 *E*), though perhaps more data are needed to determine the exact form of this decrease. However, SAXRD analysis and TEM images (Fig. 4 *D*) show that the LPNs are shorter than with taxol, indicating that taxol mainly stabilized the straight curvature of the tubulin subunits along the PFs, thereby leading to longer polymers. This is complementary to our earlier osmotic stress measurements (15), which showed that taxol does not change the lateral interactions between PFs.

The second difference is that in the absence of taxol, $\langle N \rangle$ is smaller than in the presence of taxol (Fig. 4, *A* and *E*). Perhaps the reason for this is that in the absence of taxol, it is somewhat easier for the complex to adjust its size, and by going to a smaller size, the matching between the charge densities of the MT and the lipid bilayer improves. Interestingly, we found that $\langle N \rangle$ increases logarithmically with the molar ratio, t, between Taxol and tubulin (Fig. 4 *D*), for $x_{CL} = 0.5$. This suggests that the stabilization of the MT PFs increases logarithmically with t, implying that taxol stabilizes the straight PF conformation in a global fashion and clearly beyond its local attachment to specific tubulin subunits, which would yield a linear dependence on t. This is consistent with the manner in which taxol suppresses MT dynamics (28); a small amount of taxol significantly suppresses MT dynamics.

To understand how MT PF number is regulated by the charge density of an enveloping layer, we provide a simple physical description of the energy associated with the coassembly of an MT with an oppositely charged lipid bilayer. The basic assumption of the model is that, even though an MT is highly resistant against deformations that require changes in PF length, the binding between two adjacent PFs in an MT is quite weak (15). As a result, even weak noncovalent interactions between an MT and the environment—such as the mechanical

torque exerted on a MT by the adhering lipid bilayer or electrostatic interactions—can alter MT PF number.

Assume that a MT consists of m negatively charged PFs of length l in the form of a circular bundle. The total PF length $L = ml$ is proportional to the number of tubulin monomers, which will be assumed fixed in the following. For a given cross section of the MT, draw a line from each PF to the center of the MT so that the angle between adjacent lines equals $2\pi/m$. Let φ^* be the preferred value of this angle in the absence of electrostatic interaction between PFs. The lateral bending energy cost of a MT, associated with change in PF number and hence deviations of $2\pi/m$ from φ^* is, to the lowest order,

$$E_{el}/l = \frac{m}{2}k\left(\frac{2\pi}{m} - \varphi^*\right)^2, \tag{3}$$

where k is an effective bending stiffness per unit length associated with variation in PF number.

The MT is surrounded by a cationic lipid bilayer with a thickness denoted by a_2. Let s be the arc-distance along the center line of this bilayer, again along a cross section (Fig. 5), and let $\rho(s)$ be the local curvature radius of the center line. The Helfrich bending energy cost of the lipid bilayer is then

$$E_l/l = \frac{\kappa}{2}\int\left(\frac{1}{\rho(s)}\right)^2 ds, \tag{4}$$

with $\kappa \sim 10\,k_BT$ the membrane bending modulus (16). We will assume that lipid material is freely exchangeable with a reservoir, so that the MT is fully covered. Equation 3 again does not include the electrostatic self-energy of the lipid material.

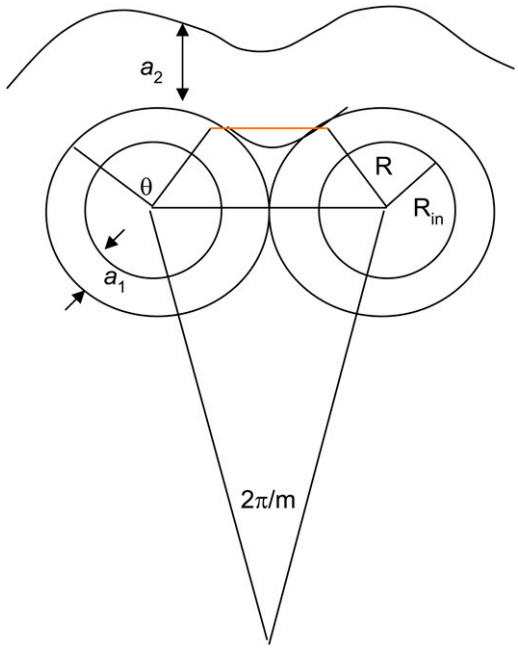

FIGURE 5 Cartoon demonstrating the geometry associated with a membrane that coats the MT PFs.

The main contribution to the gain in electrostatic energy of the system comes from the free energy gain due to the counterion release(39) that produced the association of the two macroions of opposite charge (the MT and the cationic lipid layer). The interface between the MT and the lipid bilayer is a cylinder of radius $R \approx ma_1$ and surface area $A \approx La_1$ (a_1 is the size of a PF monomer). The net surface charge density, σ_{cyl}, of the cylinder at the interface between the MT and the lipid layer depends on the mole fraction, x_{CL}, of cationic lipid in the membrane as

$$\sigma_{cyl} = -c\sigma_{MT}a_1 + 0.5x_{CL}\sigma_{cat}a_2 \approx (-c + 1.4x_{CL})e/\mathrm{nm}^2. \tag{5}$$

Here, σ_{cat} and σ_{MT} are, respectively, the charge densities per unit volume of a completely cationic lipid bilayer and of the MT wall, c is the fraction of total MT wall charge per unit area that is at the interface between the MT wall and the lipid bilayer, and the factor 0.5 reflects the symmetry of the lipid bilayer, i.e., only half of the membrane charge is located at the interface between the membrane and the MT and the other half is at the external lipid bilayer. The mole fraction at the isoelectric point is $x_{iso} = ca_1\sigma_{MT}/0.5a_2\sigma_{cat} \approx 0.7c$ under the conditions of our experiments, described in Materials and Methods.

The entropic free-energy gain due to counterion release will be included as an adhesion energy per unit area γ between the lipid bilayer and the oppositely charged PF (39). This counterion-release adhesion energy is of the order of the thermal energy times the number of charges per unit area in the contact region between the two macroions, i.e., $\gamma = \gamma_0 + p(k_BTa_2\sigma_{cat}/e)x_{CL} \approx \gamma_0 + p(3\,\mathrm{nm}^{-2}) \times k_BTx_{CL}$. The constant γ_0 is included to allow for any residual van der Waals attraction between lipid and tubulin material, and p is the fraction of counterions that are released.

An important point of the model is that when we evaluate the adhesion energy, we should not treat the MT as circular, but must account for the surface structure of the MT provided by the individual PFs. As the lipid bilayer wraps around the profile of the MT, sections that adhere to a PF will alternate with sections, between PFs, that do not adhere, since the bending stiffness of the bilayer prevents it from perfect local adjustment to the MT surface profile.

Let θ be the arc distance of the contact line between the lipid bilayer and one PF (in cross section). If we approximate a PF cross section as circular, with radius a, then the adhesive contact area per PF equals $la\theta$, so the total contact area per MT is $La\theta$. The adhesion energy is then

$$E_{ad} = -\lambda L - \gamma\theta aL. \tag{6}$$

The first term, with λ equal to γ times a microscopic length, is the adhesion energy per unit length between a locally flat lipid bilayer and a PF.

We now can minimize the bending energy (Eq. 4) of the bilayer sections between the PFs if we know the cross-sectional shape of a PF. For PFs with a circular cross section

with radius a, this is a straightforward calculation with the following result:

$$\frac{a}{\kappa L}E_{\mathrm{tot}}(m,\theta) = -\frac{\lambda a}{\kappa} - \left(\frac{\gamma a^2}{\kappa} - \frac{1}{2}\right)\theta + \frac{\tan^2(\theta/2 - \pi/m)}{(1 - \sin(\theta/2 - \pi/m))} + \frac{ak}{2\kappa}\left(\frac{2\pi}{m} - \varphi^*\right)^2, \quad (7)$$

where all terms are dimensionless. The first term is the adhesive line energy, the second term is the sum of the adhesive surface energy and the bending energy of the adhering lipid bilayer. The third term is the bending energy of the connecting nonadhering sections, and the fourth term is the sum of the MT bending and electrostatic energies. The effective MT bending stiffness per unit length, k, and the preferred angle between protofilaments, φ^*, are in principle functions of σ_{cyl}, although in our experiment, the screening condition is strong. The Debye-Huckel electrostatic screening radius is typically ~1 nm (see Fig. 4 *A*) and thus much smaller than the thickness of the lipid bilayer and the PF diameter. In this case, the dependence of k and φ^* on σ_{cyl} is very weak. In the discussion below, to the lowest order, we ignore this dependence and regard k and φ^* as constants.

This result can be viewed as a variational expression that must be minimized with respect to the adhesion angle θ. The outcome of this minimization depends on the key dimensionless parameter

$$\Gamma(x_{\mathrm{CL}}) = \frac{\gamma a^2}{\kappa} = \frac{k_{\mathrm{B}}Ta_2p\sigma_{\mathrm{cat}}a^2}{\kappa e}x_{\mathrm{CL}} \approx 2px_{\mathrm{CL}}. \quad (8)$$

When $\Gamma = 1/2$, a continuous transition takes place from an adhesive to a nonadhesive state.

When $\Gamma < 1/2$ (corresponding to membranes with low charge density, $x_{\mathrm{CL}} < 1/4p$), a ''weak-adhesion'' regime, the bending energy of the lipid bilayer exceeds the adhesion energy, and Eq. 3 is minimized by $\theta = 0$. The lipid bilayer is either a perfect cylinder, only touching each of the PFs in turn, or it does not adhere at all to the MT (i.e., the lipid vesicles stick to the MT, forming a ''beads on a rod'' structure (16)). In this case, the total energy reduces to:

$$E_{\mathrm{tot}}(m)a/\kappa L \approx -\frac{\lambda a}{\kappa} + (\pi/m)^2 + \frac{ka}{2\kappa}\left(\frac{2\pi}{m} - \varphi^*\right)^2. \quad (9)$$

The first term, the contact-line energy, is the only negative contribution. For adhesion, the total energy must be negative, so $\lambda a/\kappa$ must exceed$(\varphi^*/2)^2$. Minimization of the energy with respect to m in that case gives, for the optimal number m^* of PFs,

$$\frac{2\pi}{m^*} = \left(\frac{ka/\kappa}{1/2 + ka/\kappa}\right)\varphi^*. \quad (10)$$

The fact that the optimal value of $2\pi/m$ is $<\varphi^*$ (corresponding to a PF number greater than that of uncoated MT) is due to the lipid bending energy, which can be reduced by increasing the radius of the MT. This result is in accordance with our findings (Fig. 3 *B*).

In the regime where $\Gamma > 1/2$, the adhesion energy of the bilayer exceeds the bending energy. The bilayer now partially follows the outer contour of the MT. The total energy, which is minimized when the arc length of the adhesive sections is $\theta(m) = 2(\Gamma + \pi/m)$, equals

$$E_{\mathrm{tot}}(m)a/\kappa L = -\frac{\lambda a}{\kappa} - \left(\Gamma - \frac{1}{2}\right)^2 - \frac{2\pi}{m}\left(\Gamma - \frac{1}{2}\right) + \frac{ka}{2\kappa}\left(\frac{2\pi}{m} - \varphi^*\right)^2. \quad (11)$$

The third term is the lipid bending energy which now favors smaller m values, since that allows for extra contact area between the bilayer and a PF. Minimization with respect to m now gives, for the optimal number m^* of PF's,

$$\frac{2\pi}{m^*} = \varphi^* + \left(\frac{\kappa}{ka}\right)\left(\Gamma(x_{\mathrm{CL}}) - \frac{1}{2}\right). \quad (12)$$

This result also predicts a decrease in the PF number with increasing membrane charge density.

By comparing Eqs. 10 and 12 with our results we find that k should be of order 10–100 $k_{\mathrm{B}}T$/nm to account for the variation we observe in MT PF number.

If we vary x_{CL}, then mainly the adhesive energy is affected. With decreasing mole fraction, the optimal number of PFs steadily increases until we reach the critical point where adhesion between the lipid bilayer and the MT is lost. Note that due to the van der Waals attraction, it is necessary to use more rigid membranes to study this ''wrapping transition'' (16). It should be noted that the physics of this wrapping transition—with its competition between adhesion

TABLE 1 The values of a_i in the case of pure MT

Parameter value	Description	Source
$a_1 = 8.13$ nm	R_1—the internal microtubule radius	Tubulin structural data (31) but allowed to fluctuate within reasonable physical limits
$a_2 = 1.58$ nm	R_2-R_1—width of the internal low electron density region	Free
$a_3 = 2.52$ nm	R_3-R_2—width of the high electron density region	Free
$a_4 = 4.9$ nm	R_4-R_1—total microtubule wall width	Tubulin structural data (31)
$a_5 = 411$ e/nm^3	Mean electron density of microtubule wall	Microtubule (31) and tubulin (40) structural data, tubulin M_W and partial specific volume (32, 41)

TABLE 2 The values of a_i in the case of the LPN

Parameter value	Description	Source
$a_1 = 8.13$ nm	R_1—the internal microtubule radius	Based on the fit to our pure microtubule scattering data but allowed to fluctuate within reasonable physical limit to allow fluctuations in the internal microtubule structure
$a_2 = 1.58$ nm	$R_2-R_1 = R_{14}-R_{13}$—width of the internal low electron density region	Based on the fit to our pure microtubule scattering data
$a_3 = 2.52$ nm	$R_3-R_2 = R_{13}-R_{12}$—width of the high electron density region	Based on the fit to our pure microtubule scattering data
$a_4 = 4.9$ nm	$R_4-R_1 = R_{14}-R_{11}$—total microtubule wall width	Tubulin structural data (31)
$a_5 = 2.8$ nm	R_8-R_7—the total length of the two lipid tails in the membrane	Lipid structural data (33, 34), but allowed to fluctuate within reasonable physical limits to account for fluctuations in the lipid layer
$a_6 = 411$ e/nm^3	Mean electron density of microtubule wall	Tubulin structural data
$a_7 =$ unknown	f—fraction of tubulin coverage on third layer	Free to float between 0 to 1
$a_8 = 400$ e/nm^3 (for DOPC 5e/nm^3 less for each 20% of DOTAP)	Mean electron density of the lipid head group	Lipid structural data (33, 34)
$a_9 = 270$ e/nm^3	$\Delta\rho_7$—Mean electron density of the lipid tail	Lipid structural data (33, 34)
$a_{10} = 333$ e/nm^3	Mean electron density of water	From the mass density of water (1 gr/cm^3)
$a_{11} = 0.3$ nm	$R_5-R_4 = R_9-R_8$—width of first constant intermediate mean electron density region of lipid head	Lipid structural data (33, 34)
$a_{12} = 0.4$ nm	$R_6-R_5 = R_{10}-R_9$—width of high constant mean electron density region of lipid head	Lipid structural data (33, 34)
$a_{13} = 0.9$ nm	$R_7-R_4 = R_{11}-R_8$—total width of lipid head group	Lipid structural data (33, 34)
$a_{14} = 1$	Fraction of lipid bilayer coverage on second layer	A fixed parameter (based on the lipid/tubulin stoichiometry, calculated as in May and Ben-Shaul (35))

energy and bending energy—is essentially similar to the well-known Marky-Manning transition of DNA/nucleosome complexation.

CONCLUSIONS

We have shown that the electrostatic interactions between a MT and a charged layer coating it influence the MT PF number in LPNs. We find that the mean PF number decreases in a stepwise fashion with the lipid-bilayer charge density. The physical model we presented to account for our results suggests that the energy associated with the PF number change is of order 10 k_BT. This model system may provide insight into one of the mechanisms through which MT size is regulated in cells. The fact that the range of charge densities that lead to each mean value of PF number is relatively broad allows variations in the composition of the MT enveloping layer while maintaining the same PF number.

APPENDIX: FORM FACTOR OF CONCENTRIC HOLLOW CYLINDERS AND ITS IMPLICATION TO MICROTUBULE AND LIPID-PROTEIN NANOTUBES

We start by considering the form factor of a single hollow cylinder of core radius R_c and shell radius R_s with a total height $2H$. We assume that the inside and outside of the tube have the same electron density and that the inside of the tube has a uniform electron density that differs by $\Delta\rho_0$ from the outside of the tube. The scattering amplitude F is proportional to the Fourier transform of the electron density of the hollow cylinder:

$$F(q_{\perp},q_z)\propto\int_V \Delta\rho_0(r)\exp(-iqr)dr,$$

TABLE 3 Calculation of R_k and ρ_k

R_k	ρ_k
$R_1 = a_1$	$\rho_1 = 0$
$R_2 = a_1 + a_2$	$\rho_2 = 2(a_6 - a_{10})a_4/(a_3 + a_4)$
$R_3 = a_1 + a_2 + a_3$	$\rho_3 = \rho_2$
$R_4 = a_1 + a_4$	$\rho_4 = \rho_1$
$R_5 = a_1 + a_4 + a_{11}$	$\rho_5 = a_{14}(2(a_8 - a_{10})a_{13} - (a_9 - a_{10})(a_{13} - a_{12} - a_{11}))/(a_{13} + a_{12})$
$R_6 = a_1 + a_4 + a_{11} + a_{12}$	$\rho_6 = \rho_5$
$R_7 = a_1 + a_4 + a_{13}$	$\rho_7 = -a_{14}(a_9 - a_{10})$
$R_8 = a_1 + a_4 + a_{13} + a_5$	$\rho_8 = \rho_7$
$R_9 = a_1 + a_4 + a_5 + 2a_{13} - a_{11} - a_{12}$	$\rho_9 = \rho_5$
$R_{10} = a_1 + a_4 + a_5 + 2a_{13} - a_{11}$	$\rho_{10} = \rho_5$
$R_{11} = a_1 + a_4 + a_5 + 2a_{13}$	$\rho_{11} = \rho_1$
$R_{12} = a_1 + a_4 + a_5 + 2a_{13} + a_4 - a_2 - a_3$	$\rho_{12} = 2a_4(a_6 - a_{10})a_7a_{14}/(a_4 + a_3)$
$R_{13} = a_1 + a_4 + a_5 + 2a_{13} + a_4 - a_2$	$\rho_{13} = \rho_{12}$
$R_{14} = a_1 + a_4 + a_5 + 2a_{13} + a_4$	$\rho_{14} = \rho_1$

where the integration is over the volume V of the hollow cylinder.

In cylindrical coordinates, we obtain

$$F(q_{\perp},q_z) \propto \Delta\rho_0 \int_{-H}^{H} dz \exp(-iq_z z) \int_{R_x}^{R_s} \rho d\rho \int_0^{2\pi} \exp(-iq_{\perp}\rho\cos(\phi)d\phi$$
$$= 4\pi\Delta\rho_0 \sin(Hq_z/q_z) \int_{R_c}^{R_s} \rho d\rho J_0(q_{\perp}\rho)$$
$$= 4\pi\Delta\rho_0 \sin(Hq_z/q_z)\{R_s J_1(q_{\perp}R_s) - R_c J_1(q_{\perp}R_c)\},$$

where J_0 and J_1 are the zero and first Bessel functions of the first kind.

The intensity I is given by $|F|^2$, but since our solutions are isotropic we need to perform a powder average in the reciprocal q space:

$$I(q) \propto \int |F|^2 d\Omega_q = \int_0^{2\pi} d\psi_q \int_0^{\pi} |F|^2 \sin\theta_q d\theta_q$$
$$= 2\pi \int_0^{\pi} |F|^2 \sin\theta_q d\theta_q.$$

By setting $x = \cos\theta_q$ we get: $q_{\perp} = q\sin\theta_q = q(1-x^2)^{1/2}$ and $q_z = q\cos\theta_q = qx$, so finally the intensity is given by

$$I(q) = A(\Delta\rho_0)^2 \int_0^1 \frac{\sin^2(Hqx)}{q^4x^2(1-x^2)}\{R_s J_1(qR_s(1-x^2)^{1/2})$$
$$- R_c J_1(qR_c(1-x^2)^{1/2})\}^2 dx + B,$$

where A and B are constants.

In the more general case, we have a series of n concentric homogenous hollow cylinders with an overall radial electron density profile given by the set of parameters (R_k, ρ_k, H_k). $(\rho_{k+1}+\rho_k)/2 = \Delta\rho_k$ is the difference between the electron density of the surrounding (the solvent in our case) and the kth homogenous hollow cylinder with a core radius R_k and a shell radius R_{k+1}. $2H_k$ is the height of the kth hollow cylinder ($H_{n+1} = 0$) and $k = 1,2,\ldots,n+1$. The scattering intensity of such randomly oriented n concentric cylinders is

$$I(q) = A \int_0^1 \frac{1}{q^4x^2(1-x^2)}$$
$$\times \left(\sum_{k=1}^{n} \sin(H_k qx) \times \Delta\rho_k \times \{R_{k+1} J_1(qR_{k+1}(1-x^2)^{1/2})\right.$$
$$\left. - R_k J_1(qR_k(1-x^2)^{1/2})\}\right)^2 dx + B.$$

For n infinitely long concentric hollow cylinders, we get

$$I(q) = A \int_0^1 \frac{1}{q^4x^2(1-x^2)}$$
$$\times \left(\sum_{k=1}^{n} \Delta\rho_k \times \{R_{k+1} J_1(qR_{k+1}(1-x^2)^{1/2})\right.$$
$$\left. - R_k J_1(qR_k(1-x^2)^{1/2})\}\right)^2 dx + B.$$

In our case, we reduced the number of parameters by having R_k, ρ_k be a function of a subset of parameters, a_i, out of which a much smaller subset of parameters was free to float.

For the case of pure microtubule solutions we have the set of parameters shown in Table 1 For the microtubule-lipid complexes the set of parameters is given in Table 2. The values of R_k and ρ_k are calculated (based on the parameters of Tables 1 and 2) as described in Table 3.

We thank K. Ewert, S. Richardson, and K. Linberg for experimental help; D. McLaren and P. Allen for help with cartoons; and M. A. Jordan, A. Gopinathan, A. Zilman, N. Gov, T. Deming, and P. Pincus for discussions.

This work was supported by National Institutes of Health grant GM-59288 (to U.R., D.J.N., Y.L., and C.R.S.), National Science Foundation grants DMR-0503347 and CTS-0404444, Dept. of Energy grant DE-FG02-06ER46314 (to U.R., D.J.N., Y.L., and C.R.S.), and National Institutes of Health grant NS13560 (to H.P.M. and L.W.). The University of California, Santa Barbara, Material Research Laboratory received support from National Science Foundation grant DMR-0080034. The Stanford Synchrotron Radiation Laboratory, where some of this work was done, is supported by the U.S. Dept. of Energy. U.R. received fellowship support from the International Human Frontier Science Program Organization and the European Molecular Biology Organization.

REFERENCES

1. Tilney, W. G., J. Bryan, D. J. Bush, K. Fujjiwara, M. S. Mooseker, D. B. Murphy, and D. H. Snyder. 1973. Microtubules: evidence for 13 protofilaments. *J. Cell Biol.* 59:267–275.
2. Pierson, G. B., P. R. Burton, and R. H. Himes. 1978. Alterations in number of protofilaments in microtubules assembled in vitro. *J. Cell. Biol.* 76:223–228.
3. Eichenlaub-Ritter, U. 1985. Spatiotemporal control of functional specification and distribution of spindle microtubules with 13, 14 and 15 protofilaments during mitosis in the ciliate *Nyctotherus*. *J. Cell Sci.* 76: 337–355.
4. Tucker, J. B., M. J. Milner, D. A. Currie, J. W. Muir, D. A. Forrest, and M. J. Spencer. 1986. Centrosomal microtubule-organizing centres and a switch in the control of protofilament number for cell surface-associated microtubules during *Drosophila* wing morphogenesis. *Eur. J. Cell Biol.* 41:279–289.
5. Mogensen, M. M., and J. B. Tucker. 1987. Evidence for microtubule nucleation at plasma membrane-associated sites in *Drosophila*. *J. Cell Biol.* 88:95–107.
6. Westermann, S., A. Avila-Sakar, H. Wang, H. Niederstrasser, J. Wong, D. G. Drubin, E. Nogales, and G. Barnes. 2005. Formation of a dynamic kinetochore-microtubule interface through assembly of the Dam1 ring complex. *Mol. Cell.* 17:277–290.
7. Miranda, J. L., P. De Wult, P. K. Sorger, and S. C. Harrison. 2005. The yeast DASH complex forms closed rings on microtubules. *Nat. Struct. Mol. Biol.* 12:138–143.
8. Unger, E., K. J. Bohm, H. Muller, H. Grossmann, H. Fenske, and W. Vater. 1988. Formation of double-walled microtubules and multilayered tubulin sheets by basic proteins. *Eur. J. Cell Biol.* 46:98–104.

9. Sackett, D. L., V. Chernomordik, S. Krueger, and R. Nossal. 2003. Use of small-angle neutron scattering to study tubulin polymers. *Biomacromolecules*. 4:461–467.
10. Bohm, K. J., W. Vater, H. Fenske, and E. Unger. 1984. Effect of mictrotubule-associated proteins on the protofilament number of microtubules assembled in vitro. *Biochim, Biophys. Acta*. 800:119–126.
11. Jacobs, M., P. M. Bennett, and M. J. Dickens. 1975. Duplex microtubule is a new form of tubulin assembly induced by polycations. *Nature*. 257:707–709.
12. Behnke, O. 1975. An outer component of microtubules. *Nature*. 257: 709–710.
13. Erickson, H. P., and W. A. Voter. 1976. Polycation-induced assembly of purified tubulin. *Proc. Natl. Acad. Sci. USA*. 73:2813–2817.
14. Needleman, D. J., M. A. Ojeda-Lopez, U. Raviv, H. P. Miller, L. Wilson, and C. R. Safinya. 2004. Higher-order assembly of microtubules by counterions: from hexagonal bundles to living necklaces. *Proc. Natl. Acad. Sci. USA*. 101:16099–16103.
15. Needleman, D. J., M. A. Ojeda-Lopez, U. Raviv, K. Ewert, J. B. Jones, H. P. Miller, L. Wilson, and C. R. Safinya. 2004. Synchrotron X-ray diffraction study of microtubules buckling and bundling under osmotic stress: a probe of interprotofilament interactions. *Phys. Rev. Lett*. 93: 198104–1.
16. Raviv, U., D. J. Needleman, Y. Li, H. P. Miller, L. Wilson, and C. R. Safinya. 2005. Cationic liposome-microtubule complexes: pathways to the formation of two-state lipid-protein nanotubes with open or closed ends. *Proc. Natl. Acad. Sci. USA*. 102:11167–11172.
17. Needleman, D. J., J. B. Jones, U. Raviv, M. A. Ojeda-Lopez, H. P. Miller, L. Wilson, and C. R. Safinya. 2005. Supramolecular assembly of biological molecules purified from bovine nerve cells: from microtubule bundles and necklaces to neurofilament networks. *J. Phys.: Cond. Matt*. 17:S3225–S3230.
18. Needleman, D. J., M. A. Ojeda-Lopez, U. Raviv, K. Ewert, J. B. Jones, H. P. Miller, L. Wilson, and C. R. Safinya. 2005. Radial distortion of microtubules by osmotic pressure and the mechanism of action of taxol and associated proteins. *Biophys. J*. 89:3410–3423.
19. Andreu, J. M., J. F. Diaz, R. Gil, J. M. Pereda, M. G. Lacoba, V. Peyrot, C. Briand, E. Towns-Andrews, and J. Bordas. 1994. Solution structure of taxotere-induced microtubule to 3 nm resolution. *J. Biochem*. (*Tokyo*). 269:31785–31792.
20. Andreu, J. M., J. Bordas, J. F. Diaz, J. Garcia de Ancos, R. Gil, F. J. Medrano, E. Nogales, E. Pantos, and E. Towns-Andrews. 1992. Low resolution structure of microtubules in solution: synchrotron x-ray scattering and electron microscopy of taxol-induced microtubule assembled from purified tubulin in comparison with glycerol and MAP-induced microtubules. *J. Mol. Biol*. 226:169–184.
21. Fernando-Diaz, J., J. M. Valpuesta, P. Chacon, G. Diakun, and J. M. Andreu. 1998. Changes in microtubule protofilament number induced by taxol binding to an easily accessible site. *J. Biochem*. (*Tokyo*). 273: 33803–33810.
22. Fernando-Diaz, J., J. M. Andreu, G. Diakun, E. Towns-Andrews, and J. Bordas. 1996. Structural intermediates in the assembly of taxoid-induced microtubules and GDP-tubulin double rings: time-resolved x-ray scattering. *Biophys. J*. 70:2408–2420.
23. Wade, R. H., and D. Chretein. 1993. Cryoelectron microscopy of microtubule. *J. Struct. Biol*. 110:1–27.
24. Chretien, D., and R. H. Wade. 1991. New data on the microtubule surface lattice. *Biol. Cell*. 71:161–174.
25. Raviv, U., D. J. Needleman, and C. R. Safinya. 2006. Cationic membranes complexed with oppositely charged microtubules: hierarchical self-assembly leading to bio-nanotubes. *J. Phys. Cond. Matt*. 18: S1271–S1279.
26. Farrell, K. W., and L. Wilson. 1984. Tubulin-colchicine complexes differentially poison opposite microtubule ends. *Biochemistry*. 23: 3741–3748.
27. Mitchison, T., and M. Kirschner. 1984. Dynamic instability of microtubule growth. *Nature*. 312:237–242.
28. Derry, B. W., L. Wilson, and M. A. Jordan. 1995. Substoichiometric binding of taxol suppresses microtubule dynamics. *Biochemistry*. 34: 2203–2211.
29. Radler, J. O., I. Koltover, T. Salditt, and C. R. Safinya. 1997. Structure of DNA-cationic liposome complexes: DNA interaction in multilamellar membranes in distinct interhelical packing regimes. *Science*. 275:810–814.
30. Fernando-Diaz, J., E. Pantos, J. Bordas, and J. M. Andreu. 1994. Solution structure of GDP-tubulin double rings to 3 nm resolution and comparison with microtubules. *J. Mol. Biol*. 238:214–225.
31. Li, H., D. J. DeRosier, W. V. Nickolson, E. Nogales, and K. H. Downing. 2002. Microtubule structure at 8Å resolution. *Structure*. 10:1317–1328.
32. Lee, J. C., R. P. Frigon, and S. N. Timasheff. 1973. The chemical characterization of calf brain microtubule protein subunits. *J. Biol. Chem*. 248:7253–7262.
33. Liu, Y. F., and J. F. Nagle. 2004. Diffuse scattering provides material parameters and electron density profiles of biomembranes. *Phys. Rev. E*. 69:040901.
34. Wong, G. C. L., J. X. Tang, A. Lin, Y. Li, P. A. Janmey, and C. R. Safinya. 2000. Hierarchical self-assembly of F-actin and cationic lipid complexes: stacked three-layer tubule networks. *Science*. 288:2035–2039.
35. May, S., and A. Ben-Shaul. 1997. DNA-lipid complexes: stability of honeycomb-like and spaghetti-like structures. *Biophys. J*. 73:2427–2440.
36. Koltover, I., T. Salditt, J. O. Radler, and C. R. Safinya. 1998. An inverted hexagonal phase of cationic liposome-DNA complexes related to DNA release and delivery. *Science*. 281:78–81.
37. Szleifer, I., A. Ben-Shaul, and W. M. Gelbart. 1990. Chain packing statistics and thermodynamics of amphiphile monolayers. *J. Phys. Chem*. 94:5081–5089.
38. Safinya, C. R., E. B. S. Sirota, D. Roux, and G. S. Smith. 1989. Universality in interaction membranes: the effect of cosurfactant on the interfacial rigidity. *Phys. Rev. Lett*. 62:1134–1138.
39. Bruinsma, R. 1998. Electrostatics of DNA cationic lipid complexes: isoelectric instability. *Eur. Phys. J. B*. 4:75–88.
40. Nogales, E., S. G. Wolf, and K. H. Downing. 1998. Structure of $\alpha\beta$ tubulin dimer by electron crystallography. *Nature*. 393:199–203.
41. Frigon, R. P., and S. N. Timasheff. 1975. Magnesium-induced self-association of calf brain tubulin. I. Stoichiometry. *Biochemistry*. 14:4559–4566.